Chemical Science

ROYAL SOCIETY OF CHEMISTRY

EDGE ARTICLE

View Article Online
View Journal | View Issue

Cite this: *Chem. Sci.*, 2025, **16**, 21573

All publication charges for this article have been paid for by the Royal Society of Chemistry

Received 8th July 2025
Accepted 7th October 2025

DOI: 10.1039/d5sc05053g

rsc.li/chemical-science

Design and synthesis of single-atom layer bimetallic clusters for dehydrogenative silylation of water and alcohols

Chunying Chen,[ab] Qijie Mo,[c] Fuzhen Li,[b] Haili Song,[b] Qingsheng Gao [d] and Li Zhang *[b]

Single-atom layer clusters (SLCs) have demonstrated high catalytic potential owing to their fully exposed metal sites, alloying effects and unique electronic structures. However, the precise fabrication of bimetallic SLCs on a support remain challenging. Herein, a range of bimetallic M^1M^2-SLCs (M^1M^2 = PdNi, PtCu, PtNi) with abundant and high-density diatomic alloy sites were precisely anchored onto carboxyl-functionalized carbon nanotubes (CNTs). Catalytic results showed that the resultant composite of PdNi-SLCs/CNTs was efficient for catalytic dehydrogenative silylation of H_2O and alcohols, giving rise to diverse silanols and alkoxysilanes, respectively, in high yields. In particular, the turnover frequency and maximum turnover number of PdNi-SLCs/CNTs-catalyzed dehydrogenative silylation of water were up to 187 s^{-1} and 964 737 based on Pd, respectively. Reaction mechanism studies revealed that the high catalytic performance was primarily attributed to the fully exposed structure of PdNi-SLCs and the cooperation between the $Pd^{\delta-}$–$Ni^{\delta+}$ bimetallic clusters with asymmetric charge distribution, in which Pd rapidly dissociated the Si–H bond of silane, while the adjacent Ni-mediated H_2O activation promoted the cleavage of the O–H bond, thereby facilitating the formation of silanol.

Introduction

Organosilicon compounds are utilized in a variety of fields such as polymers, sealants, adhesives, coatings, surface treatment agents and medicine.[1–4] To synthesize silicon-based compounds, silanes are usually used as the precursors, which undergo Si–H bond activation and then furnish the functionalization.[5–10] Benefiting from the synergistic effects of dual metals, bimetallic catalysts could exhibit high efficiency in the functionalization of silanes.[11–13] The electronegativity difference induces asymmetric charge sites, which can facilitate the cleavage of the polar Si–H bond to give surface-adsorbed hydride and silyl moieties.[14] Besides, the dual metal sites could cooperatively adsorb and activate the substrates such as water, alcohol, amine, alkene and alkyne, and then promote the coupling of silyls and substrates to generate the desired silicon-containing products.[15]

Single-atom catalysts (SACs) have emerged as a class of heterogeneous catalysts due to their 100% atomic utilization efficiency and high catalytic activity.[16–31] As a derivative of SACs, bimetallic single-atom layer catalysts (SLCs) hold high potential in enhancing catalytic performances through integrating the advantages of SACs and bimetallic alloy catalysts.[32–35] Bimetallic SLCs feature highly exposed metal sites and alloyed metal atoms with electronic interactions, which not only preserve the alloying effect but also promote the contact between metal atoms and substrate molecules. To date, most developed SLCs are based on monometallic systems, whereas the development of alloyed SLCs remains limited.[36–46] This is primarily due to the tendency of heterometallic atoms to aggregate into nanoparticles *via* conventional synthesis methods, such as wet impregnation and high-temperature calcination.[34] Furthermore, the use of physically mixed metal salts as precursors in the synthesis of bimetallic SLCs often results in the randomly dispersed metal atoms, which limits their catalytic activity and applications in cooperative catalysis due to the insufficient density of alloyed diatomic sites (Fig. 1a). Therefore, to fully exploit the advantages of bimetallic SLCs, it is required to develop synthesis strategies that maximize the density of diatomic sites.[15]

Herein, a series of bimetallic M^1M^2-SLCs (M^1M^2 = PdNi, PtCu, PtNi) were precisely immobilized onto the carboxyl-functionalized carbon nanotubes (CNTs) through a two-step process, including the pre-coordination of heteronuclear

[a]*Northeast Guangdong Key Laboratory of New Functional Materials, School of Chemistry and Environment, Jiaying University, Meizhou, 514015, China*
[b]*School of Chemistry, Sun Yat-Sen University, Guangzhou 510006, China. E-mail: zhli99@mail.sysu.edu.cn*
[c]*School of Food & Pharmaceutical Engineering, Zhaoqing University, Zhaoqing, 526061, China*
[d]*College of Chemistry and Materials Science, Jinan University, Guangzhou 511443, China*

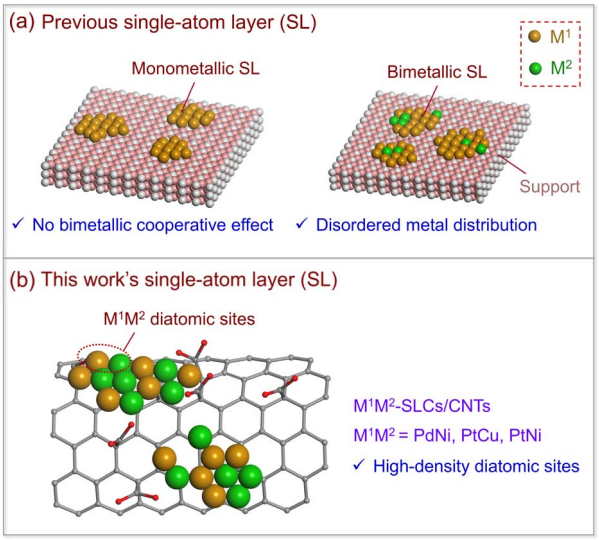

Fig. 1 Schematic comparison of the previous (a) and our developed (b) single-atom layer catalysts.

bimetallic $M^1M^2(OAc)_4$ with CNTs and the subsequent self-assembly (Fig. 1b). The resultant PdNi-SLCs/CNTs exhibited highly exposed and high-density $Pd^{\delta-}$–$Ni^{\delta+}$ diatomic sites with an asymmetric charge distribution, and displayed exceptional catalytic performance in dehydrogenative silylation of H_2O and alcohols. In particular, the turnover frequency (TOF) and maximum turnover number (TON) for dehydrogenative silylation of H_2O could reach up to 187 s^{-1} and 964 737 based on Pd, respectively. Mechanistic studies on dehydrogenative silylation of H_2O disclosed that the Si–H bond of silanes was rapidly dissociated by electron-rich Pd atoms, whose electron density was enhanced through accepting electrons from both the CNTs and neighboring Ni atoms. Meanwhile, the adjacent positively charged Ni atoms (more than +2 valence) showed high affinity to H_2O molecules, displayed strong capacity for H_2O adsorption and activation, and lowered the energy barrier for O–H bond cleavage, which was identified as the rate-determining step of the reaction. These results indicate the advantages of bimetallic sites within a layer in cooperative catalysis.

Experimental

Synthesis of PdNi-SLCs/CNTs

Prior to the synthesis of M^1M^2-SLCs/CNTs (M^1M^2 = PdNi, PtCu, PtNi), $M^1M^2(OAc)_4$ was synthesized according to the literature (Fig. S1–S3).[47,48] Afterwards, the synthesis of PdNi-SLCs/CNTs was presented as a typical example. Carboxyl-functionalized carbon nanotubes (CNTs, 100 mg) were dispersed in *N*,*N*-dimethylacetamide (DMA, 10 mL), followed by the addition of $PdNi(OAc)_4$ (1.5 mg, 0.0038 mmol). The mixture was stirred at 60 °C for 8 h and then centrifuged. The resultant solid was sequentially washed with DMA and acetone. After drying under vacuum for 1 h, the solid was heated at 180 °C for 4 h under a mixed gas flow of H_2/Ar with 5% H_2 concentration. After that, the resultant black powder of PdNi-SLCs/CNTs (94 mg) was collected for further use.

Catalytic dehydrogenative silylation of H_2O

Typically, a mixture of dimethyl(phenyl)silane (**1a**, $PhMe_2SiH$, 27.3 mg, 0.2 mmol), deionized water (0.5 mL) and PdNi-SLCs/CNTs (0.5 mg, 0.0048 mol% Pd) in acetone (2 mL) was stirred at room temperature under open-air conditions. After 1.5 min, the reaction mixture was centrifuged and purified by flash chromatography to afford the pure product dimethyl(phenyl) silanol (**2a**, 28.3 mg, 93% yield). ^{1}H NMR (400 MHz, DMSO-d_6) of **2a**: δ 7.57–7.54 (2H, m, Ar*H*), 7.37–7.34 (3H, m, Ar*H*), 5.87 (1H, s, O*H*), 0.25 (6H, s, CH_3). ^{13}C NMR (100 MHz, DMSO-d_6) of **2a**: δ 141.00, 133.36, 129.47, 128.05, 1.05.

Catalytic dehydrogenative silylation of alcohols

Typically, a mixture of $PhMe_2SiH$ (**1a**, 27.3 mg, 0.2 mmol), methanol (0.5 mL) and PdNi-SLCs/CNTs (0.5 mg, 0.0048 mol% Pd) in acetone (2 mL) was stirred at room temperature under open-air conditions. After 1.5 min, the reaction mixture was centrifuged and purified by flash chromatography to afford the pure product dimethyl(phenyl)(methoxy)silane (**2j**, 36.1 mg, 92 yield). ^{1}H NMR (400 MHz, $CDCl_3$) of **2j**: δ 7.64–7.59 (2H, m, Ar*H*), 7.44–7.40 (3H, m, Ar*H*), 3.47 (1H, s, OCH_3), 0.41 (6H, s, CH_3). ^{13}C NMR (100 MHz, $CDCl_3$) of **2j**: δ 137.46, 133.48, 129.66, 127.90, 50.67, 2.32.

DFT calculations

First-principles calculations for cell and geometry optimization were conducted using the QUICKSTEP module of the CP2K code (2024).[49] The energies and optimized geometries were determined through a hybrid Gaussian-plane-wave (GPW) approach. The calculations employed the Perdew–Burke–Ernzerhof (GGA-PBE) functional expanded in an atom-centered double-zeta molecularly optimized Gaussian basis set with Goedecker–Teter–Hutter (DZVP-MOLOPT-GTH).[50,51] The pseudopotentials for all atoms were adopted from Goedecker, Teter, and Hutter (GTH), with a plane-wave cutoff energy of 600 Ry and a reciprocal space cutoff of 60 employed in the calculations. The CP2K input file was generated using the Multiwfn software (Tian Lu), a third-party computational tool.[52] The geometry optimization was restricted to a Monkhorst–Pack *k*-point mesh of 2 × 2 × 1. Following geometry optimization, the electron transfer between Pd and Ni atoms was analyzed by calculating charge density differences of the Pd and Ni atomic models before and after two-electron charging.[53,54]

Results and discussion

Synthesis and characterization

Precise control over the local concentration of metal precursors on the support is the key to synthesize atomically dispersed catalysts. In this regard, the synthesis started with the pre-coordination of a heteronuclear bimetallic complex of $PdNi(OAc)_4$ onto carboxyl-functionalized CNTs through carboxylate exchange under solvothermal conditions (Fig. 2a). To confirm the pre-coordination of $PdNi(OAc)_4$ with CNTs, the content of carboxyl groups on CNTs was monitored using Raman spectroscopy before and after grafting with $PdNi(OAc)_4$.

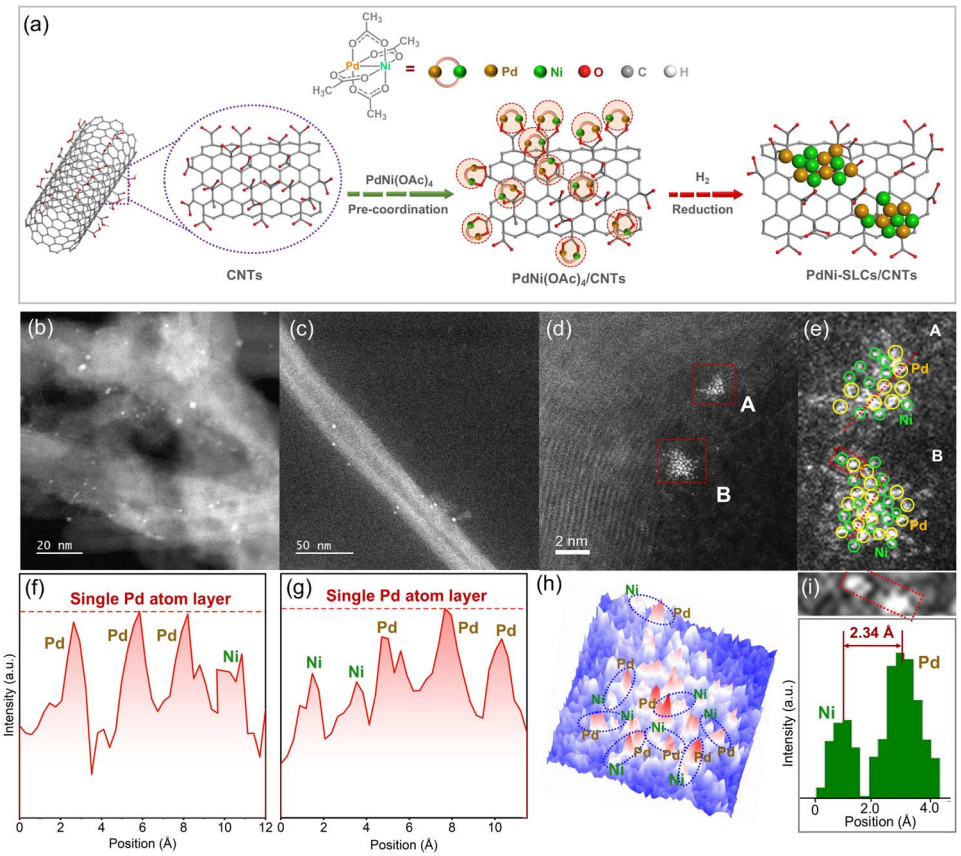

Fig. 2 Schematic illustration of the synthesis of PdNi-SLCs/CNTs (a). HAADF-STEM images of PdNi-SLCs/CNTs (b and c). The enlarged images of partial PdNi-SLCs (d and e), in which Pd and Ni single atoms are marked with yellow and green cycles, respectively. Intensity profile along the line of PdNi-SLCs in region A (f) and region B (g). Atomic intensity diagram of PdNi-SLCs in region B (h). The interatomic distance measurement of the chosen site in region B (i).

As shown in Fig. S4, the peak intensity at 795.5 cm^{-1} assigned to the bending vibration of hydroxyl groups within carboxyl groups decreased after the modification with $PdNi(OAc)_4$, suggesting an interaction between $PdNi(OAc)_4$ and CNTs. This conclusion was further supported by the release of CH_3COO^- from the reaction mixture of $PdNi(OAc)_4$ and CNTs based on the ion chromatography analysis (Fig. S5). The formation energy of $PdNi(OAc)_4$/CNTs was calculated by density functional theory (DFT) to be a negative value of −53.7 kJ mol^{-1}, implying that the carboxylate exchange between $PdNi(OAc)_4$ and CNTs was a thermodynamically favorable process (Fig. S6).

Subsequently, upon high temperature reduction with H_2, the pre-coordinated $PdNi(OAc)_4$ self-assembled into single-atom layer clusters (SLCs), giving rise to PdNi-SLCs/CNTs (Fig. 2a). The powder X-ray diffraction (PXRD) patterns of the as-prepared PdNi-SLCs/CNTs exhibited characteristic peaks corresponding to CNTs, while no diffractions associated with Pd or Ni NPs were observed, indicative of the highly dispersed nature of the Pd and Ni species within the sample (Fig. S7).[55] Therefore, this strategy not only enabled the precise dispersion of the precursors but also prevented their aggregation into nanoparticles (NPs), which usually happened under a high local concentration.

Aberration-corrected high-angle annular dark-field scanning transmission electron microscopy (AC-HAADF-STEM) images of PdNi-SLCs/CNTs revealed that the metal clusters were uniformly distributed on CNTs (Fig. 2b and c). Through high-resolution analysis, it was disclosed that the metal clusters on the support existed as exposed single-atom clusters, comprising Pd and Ni single atoms, as highlighted by yellow and green cycles, respectively (Fig. 2d and e). Considering that these were complex systems, some degree of cluster heterogeneity could not be completely avoided, and in some cases, the central region of a cluster was brighter than the edge.

To further disclose the structure, the linear intensity profiles across the clusters in regions A and B revealed a distinct difference in intensity between Pd and Ni atoms due to their difference in atomic number, while the relatively uniform intensity distribution among the Pd atoms further demonstrated the very low thickness of the clusters (Fig. 2f and g).[41,43,56] It was noted that the measured cluster thickness by atomic force microscopy (AFM) was approximately 5.8 Å, which was aligned with the combined height of a single-atom layer (~3.0 Å) and a surface carboxyl group layer (~2.5 Å), further demonstrating the single-atom layer structure of PdNi-SLCs (Fig. S8). A very minor three-dimensional (3D) cluster population was observed

after continuous efforts to identify 3D particles in the as-prepared PdNi-SLCs/CNTs.

The atomic intensity diagram of the cluster in region B clearly visualized the presence of abundant and high-density diatomic Pd–Ni sites within the cluster (Fig. 2h). The interatomic distance of adjacent Pd and Ni in the chosen site of region B was measured to be 2.34 Å, which was close to the reported Pd–Ni bond length of 2.53 Å in PdNi alloys, thus providing strong evidence for the alloying of Pd and Ni in PdNi-SLCs/CNTs (Fig. 2i).[57] The content of Pd and Ni in PdNi-SLCs/CNTs was determined to be 0.21 wt% and 0.12 wt% using an inductively coupled plasma atomic emission spectrometer (ICP-AES), respectively, revealing a near 1 : 1 Pd/Ni atomic ratio.

X-ray absorption near-edge structure (XANES) spectroscopy was performed to determine the oxidation states of Pd and Ni in PdNi-SLCs/CNTs. The Pd K-edge XANES spectrum showed an adsorption edge energy positioned between those of Pd foil and PdO, implying that the valence of Pd ranged from 0 to +2 (Fig. 3a). For the Ni K-edge XANES spectrum, PdNi-SLCs/CNTs exhibited a higher adsorption edge energy compared to NiO, indicating that the valence of Ni within PdNi-SLCs/CNTs was larger than +2 (Fig. 3b). Furthermore, high-resolution X-ray photoelectron spectroscopy (XPS) of Pd 3d and Ni 2p regions exhibited the binding energies of 336.28 eV and 856.63 eV for Pd $3d_{5/2}$ and Ni $2p_{3/2}$, respectively. The binding energy of Pd $3d_{5/2}$ fell between those of metallic Pd(0) and PdO, while the binding energy of Ni $2p_{3/2}$ was higher than that of NiO, which was consistent with the XANES results (Fig. S9).[58–60] The higher oxidation state of Ni relative to Pd suggested the presence of an asymmetric charge distribution in the $Pd^{\delta-}$–$Ni^{\delta+}$ bimetallic sites within PdNi-SLCs.

To investigate the local coordination environment of Pd and Ni atoms, extended X-ray absorption fine structure (EXAFS) spectra of PdNi-SLCs/CNTs were examined. A peak at 1.46 Å assigned to Pd–O scattering in the first coordination shell was observed, along with a secondary peak at 2.52 Å corresponding to Pd–Ni/Pd bonding (Fig. 3c). Regarding the Ni K-edge EXAFS spectra of PdNi-SLCs/CNTs, in addition to a prominent peak at 1.55 Å associated with the first shell of Ni–O scattering, two concomitant peaks at 2.17 and 2.71 Å were detected in the second coordination shell, which are supposed to be attributed to the Ni–Ni and Pd–Ni scatterings, respectively (Fig. 3d).

The coordination configuration of the Pd atom within PdNi-SLCs/CNTs was determined through the Pd K-edge EXAFS curve-fitting analysis. The coordination numbers of Pd–O, Pd–Pd and Pd–Ni bonds were found to be 1.1, 1.5, and 2.0, respectively, with corresponding bond lengths of 2.04 Å, 2.70 Å, and 2.81 Å (Fig. 3e and Table S1). The fitting results of the Ni K-edge EXAFS curve revealed the coordination numbers of 4.3, 1.3, and 2.5 for Ni–O, Ni–Ni, and Pd–Ni bonds, respectively, with bond lengths of 2.01, 2.57, and 2.87 Å (Table S2). It was noted that the fitting results for the Pd–Ni paths in the Pd-EXAFS analysis were nearly identical to those obtained from the Ni-EXAFS fitting. These results suggested that each Pd atom was

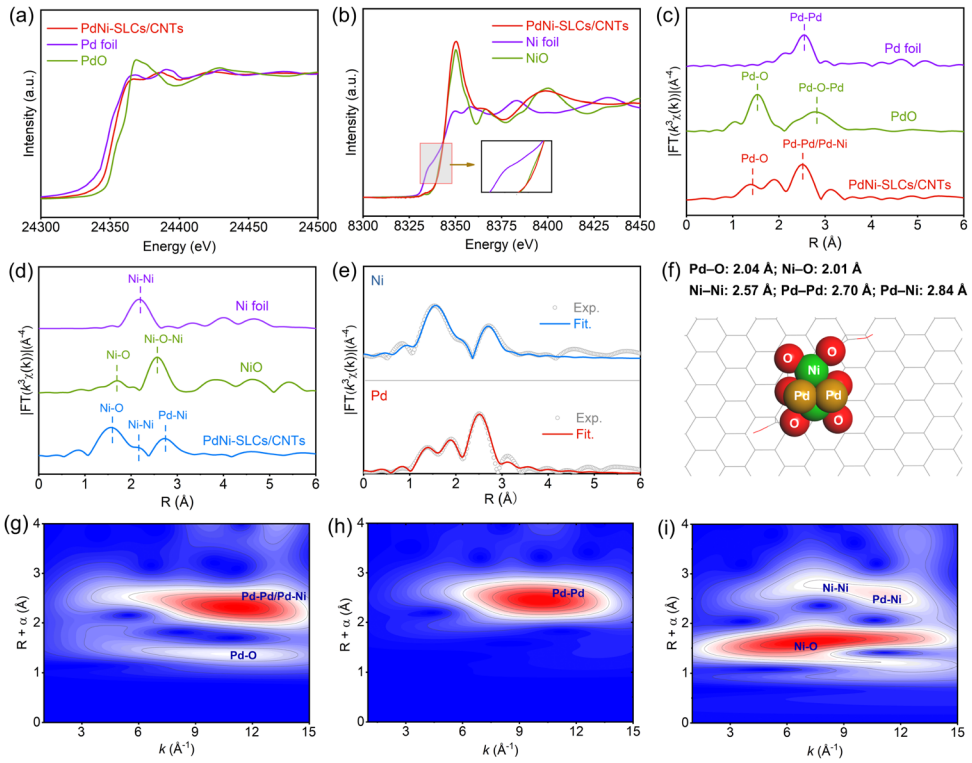

Fig. 3 Pd K-edge XANES spectra of Pd foil, PdO and PdNi-SLCs/CNTs (a). Ni K-edge XANES spectra of Ni foil, NiO and PdNi-SLCs/CNTs (b). Pd K-edge EXAFS spectra (c) of Pd foil, PdO and PdNi-SLCs/CNTs. Ni K-edge EXAFS spectra (d) of Ni foil, NiO and PdNi-SLCs/CNTs. EXAFS *R* space fitting curve of PdNi-SLCs/CNTs (e). Proposed structure of PdNi-SLCs (f). WT-EXAFS spectra of Pd K-edge of PdNi-SLCs/CNTs (g), Pd foil (h) and Ni K-edge of PdNi-SLCs/CNTs (i).

coordinated with one O atom, one Pd atom and two Ni atoms, while each Ni atom was coordinated with four O atoms, one Ni atom and two Pd atoms, suggesting that the PdNi cluster adopted a $Pd_2Ni_2O_6$ structure in average (Fig. 3f). Furthermore, wavelet transformation (WT) contour plots of both Pd and Ni for PdNi-SLCs/CNTs displayed the characteristics centers of metal–oxygen, homometallic and heterometallic bonds (Fig. 3g–i and S10).

In the synthesis of PdNi-SLCs/CNTs, the pre-dispersion of bimetallic PdNi complexes onto CNTs through carboxylate exchange played a critical role. For comparison, when non-carboxyl-functionalized CNTs were employed, PdNi alloy nanoparticles were generated after H_2 reduction on the surfaces of CNTs (named PdNi-NPs-1/CNTs), because the precursor of $PdNi(OAc)_4$ was only physically adsorbed onto the support of CNTs, and therefore the local precursor concentration couldn't be well controlled (Fig. S11a and b). On the other hand, when carboxyl-functionalized CNTs were utilized, but the physical mixture of $Pd(OAc)_2$ and $Ni(OAc)_2$ was used instead of $PdNi(OAc)_4$, PdNi alloy nanoparticles were formed again on CNTs (named PdNi-NPs-2/CNTs) upon the similar reduction treatment (Fig. S11c and d). Compared to PdNi-SLCs/CNTs, the PXRD patterns of PdNi-NPs-1/CNTs and PdNi-NPs-2/CNTs exhibited distinct peaks at 44.36° and 44.17°, respectively, which were slightly lower than the diffraction angle of the Ni (111) crystal plane (44.51°), further confirming the formation of PdNi alloy nanoparticles within these two materials (Fig. S12).[61] To further understand the unique role of CNTs, carboxyl-functionalized activated carbon (AC) was used as a comparative support to prepare PdNi-SLCs; however, PdNi-NPs/AC were achieved instead (Fig. S13). This result suggested that a uniform and well-ordered carbon support surface might play a critical role in promoting the formation of single-atom layer clusters.[62]

Based on the above results, the isolated-island morphology of the PdNi single-atom layer clusters might be related to the homogeneity of the surface carboxyl-functionalization. Firstly, the uniform distribution of carboxyl groups on the carbon nanotubes (CNTs) enabled well-dispersed anchoring of the metal precursor $PdNi(OAc)_4$, preventing localized high concentrations of the precursor. Secondly, the reduction process was carried out at a relatively low temperature (180 °C under a 5% H_2 atmosphere), which was sufficient to reduce the metal precursors but limited their long-distance migration. This controlled reduction kinetics effectively inhibited sintering. Thirdly, the strong metal–support interaction between the metal atoms and the carboxyl groups on the CNTs stabilized the reduced metal species during the reaction. As a result, the precursors within localized regions self-assembled into isolated clusters without further aggregation into larger nanoparticles, leading to the formation of the observed island-like single-atom layer structures.

In addition to PdNi-SLCs/CNTs, other bimetallic SLCs, such as PtCu-SLCs and PtNi-SLCs, were successfully fabricated on CNTs (Fig. S7). The magnified AC-HAADF-STEM images of PtCu-SLCs/CNTs and PtNi-SLCs/CNTs disclosed that bimetallic clusters in a single-atom layer structure were anchored on the CNTs, with the presence of a certain number of Pt–Cu and Pt–Ni diatomic sites, respectively (Fig. S14 and S15). These results disclosed the flexibility and versatility of the heteronuclear bimetallic complex pre-coordination and self-assembly strategy in producing various bimetallic SLCs with abundant and high-density diatomic sites.

Catalytic dehydrogenative silylation of water and alcohols

Silanols have emerged as a class of highly versatile and valuable precursors, owing to their extensive applications in organic synthesis.[63] These compounds are typically prepared through the oxidation of silanes, a process that utilizes cost-effective and eco-friendly oxidants such as water, hydrogen peroxide, or molecular oxygen.[63–67]

In this study, the selective dehydrogenative silylation of H_2O with dimethyl(phenyl)silane (**1a**) to form dimethyl(phenyl)silanol (**2a**) was employed to evaluate the catalytic performance of the as-synthesized catalysts (Table 1). PdNi-SLCs/CNTs could greatly speed up the reaction with vigorous bubbles bursting out, giving rise to the product **2a** in 98% yield at room temperature (entry 1). For comparison, PtNi-SLCs/CNTs and PtCu-SLCs/CNTs exhibited much lower reactivity with only 3.1% and 3.7% yields, respectively, in 20 min (entries 2 and 3). Even when the reaction time was elongated to 12 h, the modest yields of 54% and 45% were achieved in the presence of PtNi-SLCs/CNTs and PtCu-SLCs/CNTs, respectively (entries 4 and 5).

To study the role of the single-atom layer structure and two metal components in PdNi-SLCs/CNTs, bimetallic PdNi-NPs/CNTs as well as monometallic Pd-SAs/CNTs and Ni-SAs/CNTs were prepared (Fig. S16 and S17). The resulting catalyst PdNi-NPs/CNTs produced **2a** in 79% yield within 20 min (entry 6). Pd-SAs/CNTs presented a modest yield of 62% after 20 min reaction (entry 7). Ni-SAs/CNTs could not promote the reaction

Table 1 Catalytic hydrosilane oxidation[a]

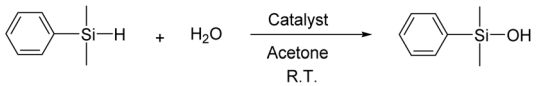

1a 2a

Entry	Catalyst	Reaction time	Yield
1	**PdNi-SLCs/CNTs**	**1.5 min**	**98%**
2	PtNi-SLCs/CNTs	20 min	3.1%
3	PtCu-SLCs/CNTs	20 min	3.7%
4	PtNi-SLCs/CNTs	12 h	54%
5	PtCu-SLCs/CNTs	12 h	45%
6	PdNi-NPs/CNTs	20 min	79%
7	Pd-SAs/CNTs	20 min	62%
8	Ni-SAs/CNTs	20 min	<1%
9	CNTs	20 min	<1%
10	—	20 min	<1%
11[b]	**PdNi-SLCs/CNTs**	**24 h**	**96%/964 734**[c]

[a] Reaction conditions: catalyst (0.5 mg), $PhMe_2SiH$ (0.2 mmol), acetone (2 mL), H_2O (0.5 mL). The yield was determined by ^1H NMR using mesitylene as an internal standard. [b] 75 mmol $PhMe_2SiH$ and 4 mg PdNi-SLCs/CNTs were used. [c] TON calculated based on the content of Pd.

at all (entry 8). The results demonstrate the critical role of the single-atom layer structure in improving catalytic efficiency.

When pristine CNTs were used as the catalyst or in the absence of any catalyst, the reaction gave a negligible yield of **2a**, revealing that the introduced metal species on CNTs were the real reaction active sites for the reaction (entries 9 and 10). Notably, the PdNi-SLCs/CNTs-catalyzed reaction was successfully scaled up to gram-level synthesis using 75 mmol of **1a**, and the desired product **2a** was obtained in 96% yield (11 g) with a high turnover number (TON) of 964 737 (entry 11). Based on the kinetic analysis of the gram-scale dehydrogenative silylation of water with substrate **1a** (7 mmol, 0.95 g), a turnover frequency (TOF) of 187 s^{-1} was determined from the slope of the fitted line using 0.0048 mol% Pd (Fig. S18).

The reaction was further carried out using $H_2{}^{18}O$, and the formation of ^{18}O-labeled **2a** was detected by high-resolution mass spectrometry, confirming that the introduced water serves as the source of the oxygen atom in the silanol product (Fig. S19).

The substrate scope of silanes was investigated using PdNi-SLCs/CNTs as the catalyst (Table 2). The catalyst showed impressive efficiency in dehydrogenative silylation of H_2O with diverse tertiary silanes, providing high yields of the corresponding silanols (**2a–2g**). It was noted that PdNi-SLCs/CNTs exhibited remarkable reaction selectivity even in the presence of a C=C double bond, as evidenced by the 90% yield of dimethyl(4-vinylphenyl)silanol (**2b**) within 15 min. Additionally, the compound 1,4-bis(dimethylsilyl)benzene, featuring two Si–H bonds, was successfully employed in PdNi-SLCs/CNTs-catalyzed dehydrogenative silylation of H_2O, affording the corresponding product **2c** in 94% yield. The catalyst was also successfully applied to the transformation of aliphatic tri(ethyl) silane to tri(ethyl)silanol (**2d**) with an 81% yield in 8 min. The reaction of H_2O with sterically hindered silanes to produce silanols, such as diphenyl(methyl)silanol (**2e**), tri(phenyl)silanol (**2f**) and tri(benzyl)silanol (**2g**), required longer reaction times and afforded satisfactory yields of 92%, 88% and 81%, respectively. Furthermore, PdNi-SLCs/CNTs exhibited high reactivity for the dehydrogenative silylation of H_2O with secondary silanes, enabling the synthesis of methyl(phenyl)silanol (**2h**) and di(phenyl)silanol (**2i**) with yields of 83% and 86%, respectively.

In addition to dehydrogenative silylation of H_2O, PdNi-SLCs/CNTs were suitable for promoting the dehydrogenative silylation of alcohols with a variety of silanes to produce alkoxysilanes (Table 2). The catalyst exhibited high reactivity for the reaction of **1a** with methanol, giving rise to the product of dimethyl(phenyl)methoxysilane (**2j**) in 92% yield. Based on the

Table 2 Substrate screening[a]

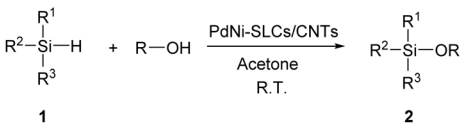

1 2

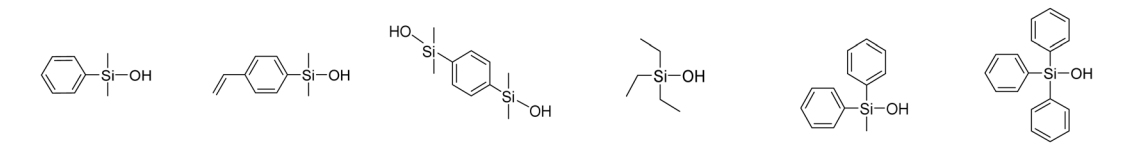

2a, 1.5 min, 93% **2b**, 15 min, 90% **2c**, 15 min, 94% **2d**, 8 min, 81% **2e**, 12 min, 92% **2f**, 1 h, 88%[b]

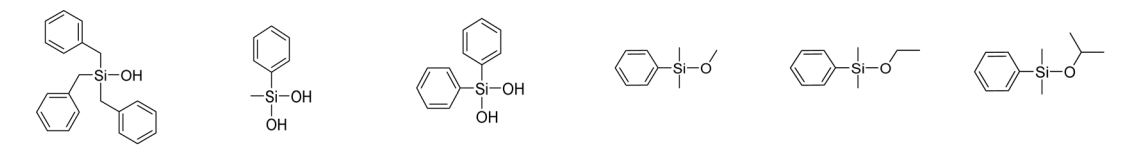

2g, 2 h, 81%[b] **2h**, 30 min, 83% **2i**, 1 h, 86% **2j**, 1.5 min, 92% **2k**, 5 min, 95% **2l**, 15 min, 87%

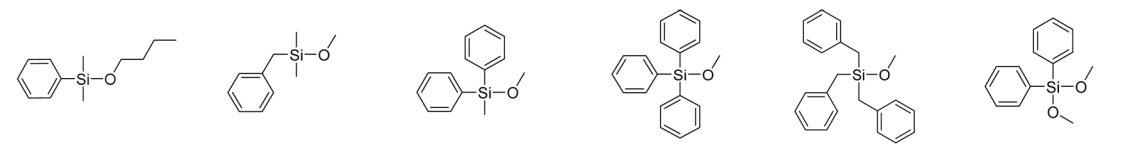

2m, 8 min, 86% **2n**, 15 min, 91% **2o**, 8 min, 85% **2p**, 1 h, 89%[b] **2q**, 1 h, 80%[b] **2r**, 30 min, 81%

[a] Reaction conditions: PdNi-SLCs/CNTs (0.0048 mol% Pd), silane (0.2 mmol), acetone (2 mL), H_2O or alcohol (0.5 mL). The yield was isolated yield.
[b] 4 mL acetone was used.

kinetic analysis of the gram-scale dehydrogenative silylation of methanol with **1a** (7 mmol, 0.95 g), a TOF up to 229 s^{-1} was achieved (Fig. S20). The catalysts also demonstrated broad applicability across a range of aliphatic alcohols, such as ethanol, isopropanol and *n*-butanol, to synthesize the desired alkoxysilanes **2k–2m** with satisfactory yields ranging from 86% to 95%. With other aromatic tertiary silanes as the dehydrogenative silylation agent, methanol was effectively converted into the target products **2n–2q** with larger than 80% yields. The dehydrogenative silylation of methanol with secondary silane of di(phenyl)silane proceeded smoothly, which furnished di(methoxy)di(phenyl)silane (**2r**) in an acceptable yield of 81%.

Recycling experiments of catalytic dehydrogenative silylation of H_2O with silane were conducted to show the robustness of PdNi-SLCs/CNTs as a heterogeneous catalyst. The catalyst retained high reactivity over 10 successive runs, demonstrating its outstanding stability (Fig. S21). The HAADF-STEM images of the recycled PdNi-SLCs/CNTs revealed that no obvious accumulation of metal clusters occurred after 10 runs (Fig. S22a and b). Furthermore, the extracted line profile of the cluster showed that the PdNi single-atom clusters remained monolayered (Fig. S22c). Inductively coupled plasma mass spectrometry (ICP-MS) analysis of the reaction filtrate after the catalytic reaction disclosed that the amounts of Pd and Ni leaching into the reaction mixture were only 0.049% and 0.18%, respectively. Additionally, the Pd $3d_{5/2}$ and Ni $2p_{3/2}$ peaks in the recycled catalyst emerged at 336.21 eV and 856.56 eV, respectively, which were close to those in the initial PdNi-SLCs/CNTs, indicating that the oxidation states of Pd and Ni did not undergo significant changes (Fig. S23).

In short, PdNi-SLCs/CNTs were an efficient heterogeneous catalyst toward dehydrogenative silylation of water or alcohols, which ranked at a high level compared with previously reported heterogeneous catalysts, owing to the fully exposed structure and the cooperative catalysis of two metals (Fig. S24, Tables S3 and S4).

Reaction mechanism studies

The activation of the Si–H bond in the initial step plays an important role in enhancing the catalytic efficiency of dehydrogenative silylation of H_2O. To elucidate the interaction between PdNi-SLCs/CNTs and silane, hydrogen–deuterium (H–D) exchange experiments were performed using $PhMe_2SiH$ (**1a**) and deuterated tri(ethyl)silane (Et_3SiD) as the model substrates. As revealed by the ^1H NMR spectra, upon mixing **1a** and Et_3SiD in the presence of PdNi-SLCs/CNTs, the Si–H signal of **1a** diminished within 3 min, while a new Si–H signal assigned to Et_3SiH emerged, indicative of the H–D exchange between **1a** and Et_3SiD (Fig. 4a). Other as-prepared catalysts, including PtNi-SLCs/CNTs, PtCu-SLCs/CNTs, Pd-SAs/CNTs and Ni-SAs/CNTs, were inactive for Si–H activation.

The state of the Si–H bond was then monitored by Fourier transform infrared (FT-IR) spectroscopy. The stretching vibration peak of the Si–H bond in the mixture of **1a** with PdNi-SLCs/CNTs disappeared, but it remained in the mixture of **1a** with CNTs (Fig. 4b). It was noted that in the Raman spectrum,

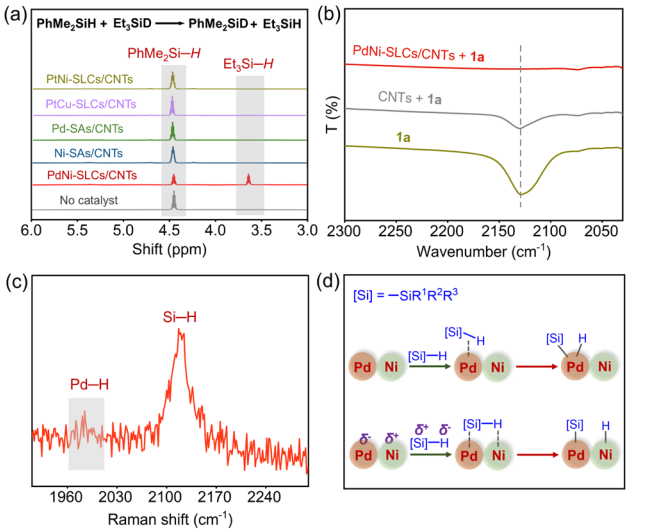

Fig. 4 H–D exchange between $PhMe_2SiH$ and Et_3SiD in the presence of different catalysts (a). ATR-IR spectra of the mixture of $PhMe_2SiH$ and PdNi-SLCs/CNTs (or CNTs) (b). Raman spectrum of the mixture of excess $PhMe_2SiH$ and PdNi-SLCs/CNTs (c). Possible Si–H coordination and dissociation modes on PdNi dual metal sites (d).

a characteristic peak corresponding to Pd–H was observed after mixing the excess **1a** with PdNi-SLCs/CNTs (Fig. 4c).

These findings showed that PdNi-SLCs/CNTs could dissociate the Si–H bond, and the bimetallic PdNi-SLCs were the activation sites.[18,67] The interaction between the Si–H bond and PdNi-SLCs might occur either on a sole Pd site or a bimetallic Pd–Ni site (Fig. 4d).[11–15] When the interaction took place on a sole Pd site, the adsorption configurations of silane molecules usually adopted a η^2-(Si–H) mode. As for the activation of the Si–H bond on a bimetallic Pd–Ni site, the $Si^{\delta+}$ and $H^{\delta-}$ atoms were expected to interact with $Pd^{\delta-}$ and $Ni^{\delta+}$ atoms, respectively, owing to the asymmetric charge distribution within the $Pd^{\delta-}$–$Ni^{\delta+}$ bimetallic site. The observation of the Pd–H bond disclosed that the Si–H bond dissociation might occur on the sole Pd site.

Density function theoretical (DFT) calculations were then conducted to analyze the adsorption of $PhMe_2SiH$ (**1a**) on PdNi-SLCs. After the adsorption of **1a**, the Si–H bond lengths (L_{Si-H}) on the sole Pd and bimetallic PdNi sites were 1.72 and 1.57 Å, respectively, in the optimized models (Fig. 5a and b). For comparison, the Si–H bond length in the free $PhMe_2SiH$ molecule was 1.48 Å. Therefore, it might be further confirmed that the Si–H bond was more inclined to dissociate on the sole Pd site rather than on the Pd–Ni bimetallic site.

To get insight into the role of Ni in the Si–H bond activation, the electronic interaction between Pd and Ni was studied. Through the differential charge density analysis of PdNi-SLCs/CNTs, it was found that the Ni atoms within PdNi-SLCs could transfer electrons to Pd atoms (Fig. 5c and S25). Further Bader charge analysis of PdNi-SLCs/CNTs disclosed that from CNTs, each Ni and Pd atom could accept 0.20 and 0.32 e^-, respectively, in average (Fig. 5d). The electron might transfer from CNTs to PdNi-SLCs and subsequently from Ni to Pd, which resulted in the electron accumulation on Pd atoms and then facilitated the Si–H bond activation and dissociation.[68,69]

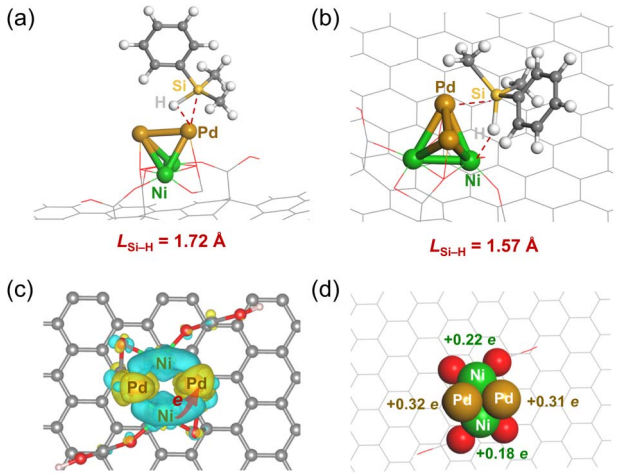

Fig. 5 Optimal structures of $PhMe_2SiH$ adsorption on PdNi-SLCs/CNTs (a and b). The brown and green atoms represent Pd and Ni atoms, respectively. Differential charge density analysis of PdNi-SLCs/CNTs (c), in which the yellow and cyan colors represent charge accumulation and consumption, respectively, and their isosurface values are all 0.0016 e $bohr^{-3}$. Bader charge analysis of Pd and Ni atoms within PdNi-SLCs/CNTs (d).

To further understand the reaction mechanism, the effects of silane and water were studied using Et_3SiD and D_2O as isotope probes. The kinetic isotope effect (k_H/k_D) for the reaction of Et_3SiD with H_2O was determined to be 1.02, suggesting that the cleavage of the Si–H bond was not the rate-determining step of the reaction (Fig. 6a and S26).[65,70] The reaction of Et_3SiH with D_2O was also conducted, and the k_H/k_D was calculated to be approximately 2.0, which disclosed that the cleavage of the O–H bond in the water might be involved in the rate-determining step (Fig. 6a).[15,71]

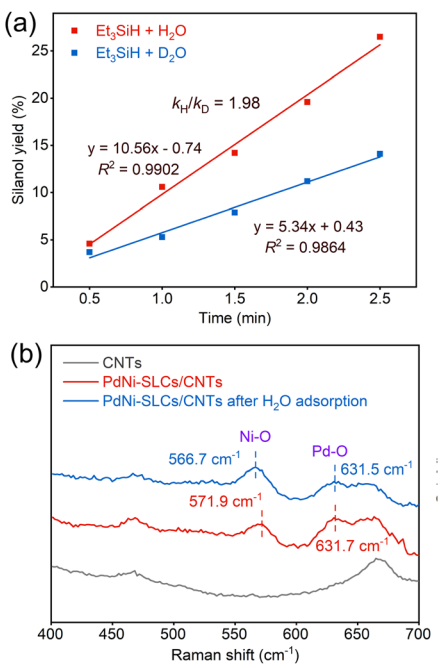

Fig. 6 KIE experiments of dehydrogenative silylation of H_2O (D_2O) with Et_3SiH using PdNi-SLCs/CNTs as the catalyst (a). Raman spectra of PdNi-SLCs/CNTs after adsorption of H_2O (b).

To study the interaction of PdNi-SLCs/CNTs and H_2O, the Raman spectra were examined (Fig. 6b). After the adsorption of water, the peak at 571.9 cm^{-1} that was assigned to the stretching vibration of the Ni–O bond in PdNi-SLCs/CNTs shifted to 566.7 cm^{-1}. The red shift of 5.2 cm^{-1} implied that the bonding strength between Ni and O atoms was weakened, which might be because the electrons transferred from the adsorbed H_2O molecule to the empty d orbitals of the highly charged Ni atom.[72] The electron donation from H_2O to the Ni atom resulted in a reduction of the Ni valence state, which could be confirmed by the lower binding energy of 0.27 eV in the XPS spectrum of PdNi-SLCs/CNTs upon water adsorption (Fig. S27a). Nevertheless, neither the stretching vibration of the Pd–O bond nor the binding energy of Pd 3d showed a noticeable shift (Fig. 6b and S27b). These results suggested that the H_2O molecule interacted more strongly with the Ni atom than with the Pd atom, and the Ni atoms in PdNi-SLCs served as the primary H_2O adsorption and activation sites for the reaction. Therefore, in PdNi-SLCs, the Pd and Ni atoms were responsible for Si–H and O–H bond activation, respectively. After the Si–H dissociation and H_2O adsorption on the Pd and Ni atoms, respectively, the formed silyl and activated H_2O interacted with each other to give the final silanol product *via* the Si–O coupling.[15]

Through experimental and theoretical studies, a plausible reaction mechanism was proposed for the typical reaction of $PhMe_2SiH$ (**1a**) and H_2O in the presence of PdNi-SLCs/CNTs. Initially, the Pd sites in PdNi-SLCs chemisorbed **1a** through a η^2-(Si–H) coordination mode, inducing the rapid dissociation of the Si–H bond to generate a metal hydride species (Pd–H) and a silyl moiety (–$SiPhMe_2$). Simultaneously, a H_2O molecule underwent chemisorption at an adjacent Ni site. The activated H_2O then attacked the resultant silyl group, leading to the formation of the silanol **2a** and Ni–H species. Finally, the adsorbed hydride on Pd and Ni sites combined to H_2, which was subsequently released from the cluster surface (Fig. 7). The

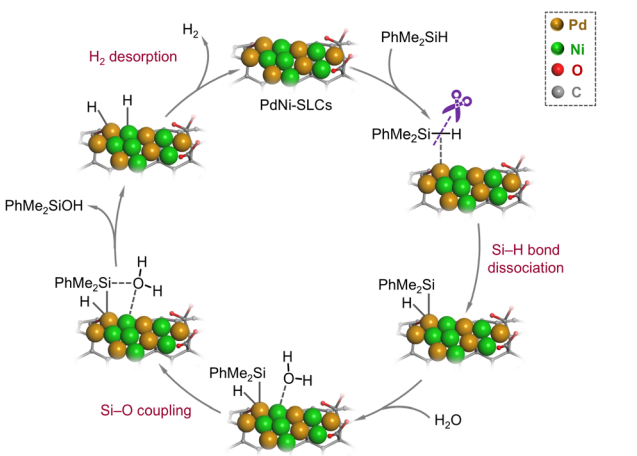

Fig. 7 Plausible reaction of dehydrogenative silylation of water catalyzed by PdNi-SLCs/CNTs.

generation of H_2 from the catalytic reaction was detected *via* gas chromatography (GC) (Fig. S28).

Conclusion

In conclusion, the fully exposed single-atom layer PdNi alloy clusters were successfully dispersed onto the CNTs *via* a newly developed strategy combining heteronuclear bimetallic complex pre-coordination and self-assembly. The PdNi-SLCs/CNTs exhibited high efficiency on catalytic dehydrogenative silylation of water or alcohols, affording diverse silanols and alkoxysilanes with high yields. The high catalytic efficiency arises from the distinctive coordination structure of PdNi-SLCs and the synergistic effect between Pd and Ni. On one hand, the fully exposed nature of the single-atom layer configuration facilitated sufficient contact between the substrates and the metal sites, thereby enhancing metal utilization and reaction rate. On the other hand, the PdNi-SLCs were enriched with $Pd^{\delta-}$–$Ni^{\delta+}$ alloy atomic pairs with asymmetric charge distribution, where the electron-rich Pd atoms were responsible for dissociating the silane, while the high-valent Ni atoms could adsorb and activate H_2O molecules. This work demonstrated the catalytic advantages of diatomic alloy sites. Further work on the synthesis of single-atom layer bimetallic catalysts and their catalytic applications is in process.

Author contributions

L. Z. conceived the idea for the project and led the project. C. C. conducted the experiments and performed the data analysis. Q. M. conducted the DFT calculations. F. L. participated in the catalyst synthesis. H. S. captured the HAADF-STEM images. Q. G. provided assistance in the preparation of the catalyst.

Conflicts of interest

The authors declare no competing financial interest.

Data availability

The authors confirm that the data supporting the findings of this study are available within the article and its supplementary information (SI). Supplementary information: general information; synthesis and characterization of catalysts (PXRD, TEM, XPS and EXAFS); catalytic dehydrogenative silylation of water and alcohols; reaction mechanism studies. See DOI: **https://doi.org/10.1039/d5sc05053g**.

Acknowledgements

The authors acknowledge support from the National Natural Science Foundation of China (22371306) and Guangdong Basic and Applied Basic Research Foundation (2019B151502017). We appreciate the support of TH-2 at the National Supercomputer Center in Guangzhou.

References

1 V. Chandrasekhar, R. Boomishankar and S. Nagendran, *Chem. Rev.*, 2006, **106**, 5847–5910.
2 L.-W. Xu, L. Li, G.-Q. Lai and J.-X. Jiang, *Chem. Soc. Rev.*, 2011, **40**, 1777–1790.
3 E. Rémond, C. Martin, J. Martinez and F. Cavelier, *Chem. Rev.*, 2016, **116**, 11654–11684.
4 Y.-J. Zuo, Z.-M. Gou, W. Quan and W.-Y. Lin, *Coord. Chem. Rev.*, 2021, **438**, 213887.
5 M. C. Lipke, A. L. Liberman-Martin and T. D. Tilley, *Angew. Chem., Int. Ed.*, 2017, **56**, 2260–2294.
6 J. M. Asensio, D. Bouzouita, P. W. N. M. van Leeuwen and B. Chaudret, *Chem. Rev.*, 2020, **120**, 1042–1084.
7 J. Y. Corey, *Chem. Rev.*, 2011, **111**, 863–1071.
8 Z. Lin, *Chem. Soc. Rev.*, 2002, **31**, 239–245.
9 L. Duarte de Almeida, H. Wang, K. Junge, X. Cui and M. Beller, *Angew. Chem., Int. Ed.*, 2021, **60**, 550–565.
10 C. He, D.-H. Si, Y.-B. Huang and R. Cao, *Angew. Chem., Int. Ed.*, 2022, **61**, e202207478.
11 Q. Chen, S. Tanaka, T. Fujita, L. Chen, T. Minato, Y. Ishikawa, M. Chen, N. Asao, Y. Yamamoto and T. Jin, *Chem. Commun.*, 2014, **50**, 3344.
12 H. Miura, K. Endo, R. Ogawa and T. Shishido, *ACS Catal.*, 2017, **7**, 1543–1553.
13 J.-W. Zhang, G.-P. Lu and C. Cai, *Green Chem.*, 2017, **19**, 2535.
14 C. Chen, Q. Mo, J. Fu, Q. Yang, L. Zhang and C.-Y. Su, *ACS Catal.*, 2022, **12**, 3604–3614.
15 L. Zhang, T. Li, X. Dai, J. Zhao, C. Liu, D. He, K. Zhao, P. Zhao and X. Cui, *Angew. Chem., Int. Ed.*, 2023, **62**, e202313343.
16 Q. Mo, L. Zhang, S. Li, H. Song, Y. Fan and C.-Y. Su, *J. Am. Chem. Soc.*, 2022, **144**, 22747–22758.
17 Q. Mo, S. Li, C. Chen, H. Song, Q. Gao and L. Zhang, *ACS Sustainable Chem. Eng.*, 2024, **12**, 6093–6101.
18 C.-Y. Chen, Q.-J. Mo, F.-Z. Li, H.-L. Song and L. Zhang, *Nano Res.*, 2024, **17**, 5914–5921.
19 S. Hu, J. Huang, M.-L. Gao, Z. Lin, Y. Qian, W. Yang, L. Jiao and H.-L. Jiang, *Angew. Chem., Int. Ed.*, 2025, **64**, e202415155.
20 S. Hu, M. Gao, J. Huang, H. Wang, Q. Wang, W. Yang, Z. Sun, X. Zheng and H.-L. Jiang, *J. Am. Chem. Soc.*, 2024, **146**, 20391–20400.
21 J. Li, J. Zhou, X.-H. Wang, C. Guo, R.-H. Li, H. Zhuang, W. Feng, Y. Hua and Y.-Q. Lan, *Angew. Chem., Int. Ed.*, 2024, **63**, e202411721.
22 Y. Zang, P. Peng, F. Pei, R.-H. Li, L. Wu, D.-Q. Lu, Y. Zhang, K. Huang, Y. Shen, Y.-H. Huang and Y.-Q. Lan, *Natl. Sci. Rev.*, 2025, **12**, nwae443.
23 E. Zhao, J. Morales-Vidal, Y. Yang, S. Mitchell, Y. Zhu, Z. Hu, J.-M. Chen, S.-C. Haw, T.-S. Chan, Z. Fan, Z.-J. Wang, N. López, J. Pérez-Ramírez and Z. Chen, *J. Am. Chem. Soc.*, 2025, **147**, 2029–2036.
24 A. Deng, E. Zhao, Q. Li, Y. Sun, Y. Liu, S. Yang, H. He, Y. Xu, W. Zhao, H. Song, Z. Xu and Z. Chen, *ACS Nano*, 2023, **17**, 11869–11881.
25 Q. Wu, J. Liang, Z.-L. Xie, Y.-B. Huang and R. Cao, *ACS Mater. Lett.*, 2021, **3**, 454–461.

26 J. Zhang, Y. Mou, W. Suo, S. Yang, J. Shen, H. Xu, Z. Zeng, R. Zhang, Z. Liang, Y. Wang, H. Zheng, J. Cao and R. Cao, *Adv. Funct. Mater.*, 2025, **35**, 2417621.
27 L. Liu, K. Yung, H. Yang and B. Liu, *Chem. Sci.*, 2024, **15**, 6285.
28 M. Kwak, J. Bok, B.-H. Lee, J. Kim, Y. Seo, S. Kim, H. Choi, W. Ko, W. H. Antink, C. W. Lee, G. H. Yim, H. Seung, C. Park, K.-S. Lee, D.-H. Kim, T. Hyeon and D. Yoo, *Chem. Sci.*, 2022, **13**, 8536.
29 Z. Xia, Y. Yin, J. Li and H. Xiao, *Chem. Sci.*, 2023, **14**, 2631.
30 N.-Y. Huang, B. Li, D. Wu, D. Chen, Y.-T. Zheng, B. Shao, W. Wang, M. Gu, L. Li and Q. Xu, *Chem. Sci.*, 2025, **16**, 1265.
31 T. Najam, S. S. A. Shah, H. Yin, X. Xiao, S. Talib, Q. Ji, Y. Deng, M. S. Javed, J. Hu, R. Zhao, A. Du, X. Cai and Q. Xu, *Chem. Sci.*, 2024, **15**, 18513.
32 X. Chen, M. Peng, X. Cai, Y. Chen, Z. Jia, Y. Deng, B. Mei, Z. Jiang, D. Xiao, X. Wen, N. Wang, H. Liu and D. Ma, *Nat. Commun.*, 2021, **12**, 2664.
33 J. Jiang, W. Ding, W. Li and Z. Wei, *Chem*, 2020, **6**, 1–17.
34 Z. Zheng, L. Qi, X. Luan, S. Zhao, Y. Xue and Y. Li, *Nat. Commun.*, 2024, **15**, 7331.
35 J. Ballesteros-Soberanas, N. Martin, M. Bacic, E. Tiburcio, M. Mon, J. C. Hernández-Garrido, C. Marini, M. Boronat, J. Ferrando-Soria, D. Armentano, E. Pardo and A. Leyva-Pérez, *Nat. Catal.*, 2024, **7**, 452–463.
36 B.-W. Zhang, L. Ren, Z.-F. Xu, N.-Y. Cheng, W.-H. Lai, L. Zhang, W. Hao, S.-Q. Chu, Y.-X. Wang, Y. Du, L. Jiang, H.-K. Liu and S.-X. Dou, *Small*, 2021, **17**, 2100732.
37 W. Liu, Z. Xiang, A. Tan, K. Wan, Z. Fu and Z. Liang, *Adv. Funct. Mater.*, 2023, **33**, 2212752.
38 S. Li, X. Guo, X. Liu and J. Shui, *ACS Catal.*, 2024, **14**, 1962–1969.
39 D. Jiang, H. Yuan, Z. Liu, Y. Chen, Y. Li, X. Zhang, G. Xue, H. Liu, X. Liu, L. Zhao and W. Zhou, *Appl. Catal., B*, 2023, **339**, 123081.
40 S. Xie, L. Liu, Y. Lu, C. Wang, S. Cao, W. Diao, J. Deng, W. Tan, L. Ma, S. N. Ehrlich, Y. Li, Y. Zhang, K. Ye, H. Xin, M. Flytzani-Stephanopoulos and F. Liu, *J. Am. Chem. Soc.*, 2022, **144**, 21255–21266.
41 Y. Si, Y. Jiao, M. Wang, S. Xiang, J. Diao, X. Chen, J. Chen, Y. Wang, D. Xiao, X. Wen, N. Wang, D. Ma and H. Liu, *Nat. Commun.*, 2024, **15**, 4887.
42 C. Dong, Z. Gao, Y. Li, M. Peng, M. Wang, Y. Xu, C. Li, M. Xu, Y. Deng, X. Qin, F. Huang, X. Wei, Y.-G. Wang, H. Liu, W. Zhou and D. Ma, *Nat. Catal.*, 2022, **5**, 485–493.
43 X. Lu, T. Luo, M. Zhang, J. H. Horton, Q. Wu, W. Wu, M. Qiao, Y. Wang and Z. Li, *Chem. Eng. J.*, 2023, **464**, 142647.
44 J. Shan, C. Ye, Y. Jiang, M. Jaroniec, Y. Zheng and S.-Z. Qiao, *Sci. Adv.*, 2022, **8**, eabo0762.
45 E. C. Kohlrausch, S. Ghaderzadeh, G. N. Aliev, I. Popov, F. Saad, E. Alharbi, Q. M. Ramasse, G. A. Rance, M. Danaie, M. Thangamuthu, M. Young, R. Plummer, D. J. Morgan, W. Theis, E. Besley, A. N. Khlobystov and J. Alves Fernandes, *Adv. Sci.*, 2025, e08034.
46 C. Chu, D. Huang, S. Gupta, S. Weon, J. Niu, E. Stavitski, C. Muhich and J.-H. Kim, *Nat. Commun.*, 2021, **12**, 5179.
47 N. Y. Kozitsyna, S. E. Nefedov, F. M. Dolgushin, N. V. Cherkashina, M. N. Vargaftik and I. I. Moiseev, *Inorg. Chim. Acta*, 2006, **359**, 2072–2086.
48 I. A. Yakushev, I. P. Stolarov, N. V. Cherkashina, A. V. Churakov, Y. V. Zubavichus, A. A. Markov, A. E. Gekhman and M. N. Vargaftik, *Inorg. Chim. Acta*, 2020, **508**, 119631.
49 J. Hutter, M. Iannuzzi, F. Schiffmann and J. VandeVondele, *Wiley Interdiscip. Rev.: Comput. Mol. Sci.*, 2014, **4**, 15–25.
50 J. P. Perdew, K. Burke and M. Ernzerhof, *Phys. Rev. Lett.*, 1996, **77**, 3865–3868.
51 J. VandeVondele and J. Hutter, *J. Chem. Phys.*, 2007, **127**, 114105.
52 T. Lu and F. Chen, *J. Comput. Chem.*, 2012, **33**, 580–592.
53 W. Tang, E. Sanville and G. Henkelman, *J. Phys.: Condens. Matter*, 2009, **21**, 084204.
54 V. Wang, N. Xu, J. Liu, G. Tang and W. Geng, *Comput. Phys. Commun.*, 2021, **267**, 108033.
55 X. Li, J. Liu, J. Wu, L. Zhang, D. Cao and D. Cheng, *ACS Catal.*, 2024, **14**, 2369–2379.
56 L. Duan, C.-T. Hung, J. Wang, C. Wang, B. Ma, W. Zhang, Y. Ma, Z. Zhao, C. Yang, T. Zhao, L. Peng, D. Liu, D. Zhao and W. Li, *Angew. Chem., Int. Ed.*, 2022, **61**, e202211307.
57 H. Wang, Q. Luo, W. Liu, Y. Lin, Q. Guan, X. Zheng, H. Pan, J. Zhu, Z. Sun, S. Wei, J. Yang and J. Lu, *Nat. Commun.*, 2019, **10**, 4998.
58 J. C. Bertolini, P. Delichere, B. C. Khanra, J. Massardier, C. Noupa and B. Tardy, *Catal. Lett.*, 1990, **6**, 215–224.
59 A. M. Venezia, R. Bertoncello and G. Deganello, *Surf. Interface Anal.*, 1995, **23**, 239–247.
60 Z. Chen, S. Li, Q. Mo, L. Zhang and C.-Y. Su, *Chin. Chem. Lett.*, 2023, **34**, 108196.
61 M. Xu, S. Dong, H. Guo, Z. Tao, Y. Jeon, Z. Zhang, Z. Chen, H. Su, Z. Liu, Y. Lin, J. T. S. Irvine, T. Li and D. Chen, *Appl. Catal., B*, 2025, **357**, 125433.
62 A. Corma, H. Garcia and A. Leyva, *J. Mol. Catal. A: Chem.*, 2005, **230**, 97–105.
63 M. Jeon, J. Han and J. Park, *ACS Catal.*, 2012, **2**, 1539–1549.
64 H. Li, L. Chen, P. Duan and W. Zhang, *ACS Sustainable Chem. Eng.*, 2022, **10**, 4642–4649.
65 K. Wang, J. Zhou, Y. Jiang, M. Zhang, C. Wang, D. Xue, W. Tang, H. Sun, J. Xiao and C. Li, *Angew. Chem., Int. Ed.*, 2019, **58**, 6380–6384.
66 F. Yang, Z. Liu, X. Liu, A. Feng, B. Zhang, W. Yang and Y. Li, *Green Chem.*, 2021, **23**, 1026.
67 F. Xie, S. Zhang, M. Yang, J. He, S. Li and Y. Zhang, *J. Am. Chem. Soc.*, 2024, **146**, 29373–29382.
68 Y. Duan, G. Ji, S. Zhang, X. Chen and Y. Yang, *Catal. Sci. Technol.*, 2018, **8**, 1039.
69 J. Dong, Y. Wang, Y.-L. Lu and L. Zhang, *Chin. Chem. Lett.*, 2023, **34**, 108052.
70 H. Liang, L.-J. Wang, Y.-X. Ji, H. Wang and B. Zhang, *Angew. Chem., Int. Ed.*, 2021, **60**, 1839–1844.
71 K. Shimizu, T. Kubo and A. Satsuma, *Chem.–Eur. J.*, 2012, **18**, 2226–2229.
72 M. Bustamante, I. Valencia and M. Castro, *J. Phys. Chem. A*, 2011, **115**, 4115–4134.